

# Separating Double-Beta Decay Events from Solar Neutrino Interactions in a Kiloton-Scale Liquid Scintillator Detector

Andrey Elagin<sup>a,\*</sup>, Henry J. Frisch<sup>a</sup>, Brian Naranjo<sup>b</sup>, Jonathan Ouellet<sup>c</sup>, Lindley Winslow<sup>c</sup>, Taritree Wongjirad<sup>c</sup>

<sup>a</sup> Enrico Fermi Institute, University of Chicago, Chicago, IL, 60637

<sup>b</sup> University of California, Los Angeles, CA, 90024

<sup>c</sup> Massachusetts Institute of Technology, Cambridge, MA 02139

<sup>d</sup> Nuclear Science Division, Lawrence Berkeley National Laboratory, Berkeley, CA 94720

---

## Abstract

We present a technique for separating double beta decay ( $\beta\beta$ -decay) events from background due to  $^8\text{B}$  solar neutrino interactions. This background becomes dominant in a kilo-ton scale liquid scintillator detector. In searches for the neutrinoless double beta decay ( $0\nu\beta\beta$ -decay)  $^8\text{B}$  background is usually considered as irreducible due to an overlap in the energy deposition. We note that in a liquid scintillator detector electrons from  $0\nu\beta\beta$ -decay often exceed Cherenkov threshold. Selection of early photons using fast photo-detectors separates prompt directional Cherenkov light from delayed isotropic scintillation light. This leads to the possibility of reconstructing the event topology of  $0\nu\beta\beta$ -decay candidate events by analyzing spatial distribution of early photons. Using a simulation of a 6.5 m radius liquid scintillator detector with 100 ps resolution photo-detectors, we perform a spherical harmonics analysis of the early light emitted in each candidate event and show the difference between  $0\nu\beta\beta$ -decay signal and  $^8\text{B}$  background events. We discuss key detector parameters that affect the separation power.

---

\*Corresponding Author: elagin@hep.uchicago.edu

19	<b>Contents</b>	
20	<b>1 Introduction</b>	<b>3</b>
21	<b>2 Detector Model</b>	<b>4</b>
22	<b>3 Kinematics and Timing of Signal and Background events</b>	<b>7</b>
23	3.1 $0\nu\beta\beta$ -decay signal and $2\nu\beta\beta$ -decay background . . . . .	7
24	3.2 $^8\text{B}$ background . . . . .	9
25	<b>4 Event Topology and Spherical Harmonics Analysis</b>	<b>11</b>
26	4.1 Topology of $0\nu\beta\beta$ -decay and $^8\text{B}$ Events . . . . .	11
27	4.2 Description of Spherical Harmonics Analysis . . . . .	12
28	4.3 Spherical Harmonics Analysis and Off-center Events . . . . .	16
29	4.4 Implementation of the spherical harmonics analysis . . . . .	17
30	<b>5 Performance of the Spherical Harmonics Analysis in Separating <math>0\nu\beta\beta</math>-decay from <math>^8\text{B}</math> Background.</b>	<b>20</b>
31	5.1 Central events with perfect vertex reconstruction . . . . .	21
32	5.2 Experimental challenges . . . . .	22
33	5.2.1 Chromatic dispersion . . . . .	23
34	5.2.2 Vertex resolution . . . . .	24
35	5.3 Requirements for the next generation liquid scintillator detectors . . . . .	26
36	<b>6 Conclusions</b>	<b>28</b>

## 1. Introduction

Over the past decade and a half, neutrino oscillation experiments have been able to conclusively establish that neutrinos have mass [1–4]. However, the nature of that mass remains one of the most fundamental open questions in particle physics. Is the neutrino unique among the Standard Model fermions with a Majorana mass [5], as is predicted by most beyond the standard model (BSM) theories, or does it have a Dirac-type mass like the rest of the fermions? A Majorana-type mass would have far reaching implications, from explaining the lightness of the neutrino and providing a bridge to higher energy phenomena through the see-saw mechanism [6, 7] to being able to provide the required lepton-number violation (LNV) and CP-violation needed for leptogenesis to explain the baryon asymmetry of the universe [8, 9]. Conversely, a Dirac neutrino mass could point to an underlying symmetry of the Universe.

Presently, the most promising technique for answering these questions is the search for Neutrinoless Double-Beta ( $0\nu\beta\beta$ ) decay [10]. In this decay, a nucleus undergoes a second order  $\beta$ -decay without producing any neutrinos,  $(Z, A) \rightarrow (Z + 2, A) + 2\beta^-$ . This is in contrast to two-neutrino double beta ( $2\nu\beta\beta$ ) decay [11], the second order Standard Model  $\beta$ -decay channel in which lepton number is conserved by the production of two anti-neutrinos,  $(Z, A) \rightarrow (Z, A + 2) + 2\beta + 2\bar{\nu}_e$ .

Liquid scintillator-based detectors have proven to be a competitive technology in this search[12]. Their primary advantage is their ease of scalability to larger instrumented masses, which involves dissolving larger amounts of the isotope of interest into the liquid scintillator (LS). This feature can allow for rapid scaling to 1 ton or more using the detectors already in operation [13]. In a large LS detector, most backgrounds can be strongly suppressed through a combination of filtration of the LS to remove internal contaminants, self-shielding to minimize the effects of external contaminants, and vetoes to reduce muon spallation backgrounds. The backgrounds relevant to  $0\nu\beta\beta$  decay which cannot be reduced through these means are the  $2\nu\beta\beta$  decay, electron scattering of  $^8\text{B}$  solar neutrinos.

The  $0\nu\beta\beta$  signal and these backgrounds have distinctive energy spectra. Since  $0\nu\beta\beta$  decay produces no neutrinos, the full energy of the decay is contained within the detector and a peak is observed around the decay  $Q$ -value. This defines a region of interest (ROI) around the  $Q$ -value. In  $2\nu\beta\beta$  decay, the neutrinos carry away some fraction of the decay energy leading to a broad spectrum of deposited energy from 0 MeV up to the decay  $Q$ -value. The interaction of  $^8\text{B}$  solar neutrinos through neutrino-electron elastic scattering (ES) produces a spectrum that rises at low energies, producing an effectively flat background in the ROI [14].

A detector with good energy resolution can statistically separate these backgrounds from the  $0\nu\beta\beta$  signal. Additional background rejection is possible with the inclusion of directional or topographical information. The two electrons emitted in  $0\nu\beta\beta$  and  $2\nu\beta\beta$  should reconstruct very differently from the single electron from  $^8\text{B}$  events. In previous work, we have shown that photo-detectors with timing resolution of  $\sim 100$  ps can be used to resolve the prompt Cherenkov photons from the slower scintillation signal and the resulting distributions can be fit for the position and direction of  $\sim\text{MeV}$  electrons[15].

In this paper, we examine in detail the time and topographical distributions of  $0\nu\beta\beta$ -decay signal and  $^8\text{B}$ background. We propose a method using spherical harmonic decomposition to analyze the distribution of early photo-electrons (PE) and use this as a discriminant. In Section 2, we describe the detector model we will use throughout this paper. Details on event kinematics and PE timing for signal and background are given in Section 3 In Section 4, we introduce the spherical harmonic decomposition, and discuss the performance of this analysis in Section 5.

## 2. Detector Model

A simulation using Geant4 version 4.9.6 is used to model a sphere of 6.5 m radius filled with liquid scintillator[16, 17]. This is the same simulation used in our preceding paper [15]. Therefore, we limit our discussion of the simulation to a summary of the most relevant simulation parameters. The scintillator composition has been chosen to match

a KamLAND-like scintillator[2]. The composition is 80% n-dodecane, 20% pseudocumene and 1.52 g/l PPO with a density of  $\rho = 0.78$  g/ml).

We use the Geant4 default liquid scintillator optical model, in which optical photons are assigned the group velocity in the wavelength region of normal dispersion. Wavelength dependent attenuation length[18], scintillation emission spectrum[18], and refractive index[19] are used. The scintillator light yield is assumed to be 9030 photons/MeV with Birks quenching ( $kB \approx 0.1$  mm/MeV)[20]. However, we do deviate from the baseline KamLAND case in that the re-emission of absorbed photons in the scintillator bulk volume and optical scattering, specifically Rayleigh scattering, has not yet been included. A test simulation shows that the effect of optical scattering is negligible [15].

In this study, we use the fact that scintillators have inherent time constants that slow this light relative to the Cherenkov light with wavelengths too long to be absorbed by the scintillator, between 360-370 nm for this scintillator. Therefore, the key inputs to the simulation are the time constants inherent to the scintillator cocktail that will determine the timing of the scintillation light relative to the unperurbed Cherenkov light. The first step in the scintillation process is the transfer of the energy deposited by the primary particles from the scintillator's solvent to the solute. The time constant of this energy transfer accounts for a rise time in scintillation light emission. Because past neutrino experiments were not highly sensitive to the effect of the scintillation rise time, there is a lack of accurate measurements of this property. We assume a rise time of 1.0 ns from a re-analysis of the data in Ref. [21] but more detailed studies are needed. The decay time constants are determined by the vibrational energy levels of the solute and are measured to be  $\tau_{d1} = 6.9$  ns and  $\tau_{d2} = 8.8$  ns with relative weights of 0.87 and 0.13 for the KamLAND scintillator[22]. In a detector of this size, chromatic dispersion, red light travelling faster than blue due to the wavelength dependent index of refraction, enhances the separation but is not the dominant effect.

The inner sphere surface is used as the photodetector. It is treated as fully absorbing, no reflections, with 100%

100 photocathode coverage. As in the case of optical scattering, reflections at the sphere are a small effect that would create  
101 a small tail at longer times. The quantum efficiency (QE) of a bialkali photocathode (Hamamatsu R7081 PMT)[23],  
102 see also Ref. [24]. We note that the KamLAND 17-inch PMTs use the same photocathode type with similar quantum  
103 efficiency. In order to neglect the effect of the transit-time-spread (TTS) of the photodetectors, we use a TTS of 0.1 ns  
104 ( $\sigma$ ), which can be achieved with large area picosecond photodetectors (LAPPDs)[25–32]. We neglect any threshold  
105 effects in the photodetector readout electronics and the photoelectron hit positions and the detection times after the  
106 TTS resolution has been applied are used for event reconstruction.

### 3. Kinematics and Timing of Signal and Background events

#### 3.1. $0\nu\beta\beta$ -decay signal and $2\nu\beta\beta$ -decay background

In both  $0\nu\beta\beta$ -decay signal and  $2\nu\beta\beta$ -decay background events near the decay energy spectrum endpoint, the kinematics of the electron pair is very similar. Large fraction of events have a nearly back-to-back topology with a close to equal energy split between electrons. To simulate  $0\nu\beta\beta$ - and  $2\nu\beta\beta$ -decay events we use a Monte Carlo generator based on phase factors from Ref. [? ]. Similarity in kinematics of  $0\nu\beta\beta$ - and  $2\nu\beta\beta$ -decay events is demonstrated in Fig. 1.

The electron angular correlations for  $0\nu\beta\beta$ -decay are noticeably different from  $2\nu\beta\beta$ -decay due to a contribution from neutrinos wave-function even at vanishingly small energies of the neutrinos [? ]. However, any practical use of this difference in separating  $0\nu\beta\beta$ -decay from  $2\nu\beta\beta$ -decay would require extremely large number of candidate events. Given half-time of  $2\nu\beta\beta$ -decay and upper limits on the half-time of  $0\nu\beta\beta$ -decay, electron angular correlations won't bring decisive separation power in controlling  $2\nu\beta\beta$ -decay background in currently planned  $0\nu\beta\beta$ -decay experiments. Excellent energy resolution at the Q-value is the key parameter in  $2\nu\beta\beta$  background suppression.

While we don't exclude that the angular correlations as an input to a multivariate technique may improve sensitivity of  $0\nu\beta\beta$ -decay searches, in this paper we assume that there is no difference in the event topology between  $0\nu\beta\beta$ - and  $2\nu\beta\beta$ -decay events. Any conclusions about  $0\nu\beta\beta$ -decay events also hold for  $2\nu\beta\beta$ -decay when total energy of the electrons in  $2\nu\beta\beta$ -decay events is close to the Q-value.

Examining the kinematics for one of the  $0\nu\beta\beta$  electrons with equal energy split, a 1.26 MeV electron travels a total path length of 0.X cm, has a distance from the origin of 0.X cm in  $0.0X \pm 0.00X$  ns and takes  $0.0X \pm 0.00X$  ns to drop below Cherenkov threshold. We note that due to scattering of the electron, the final direction of the electron before it stops does not correspond to the initial direction; however the scattering angle is small while the majority of

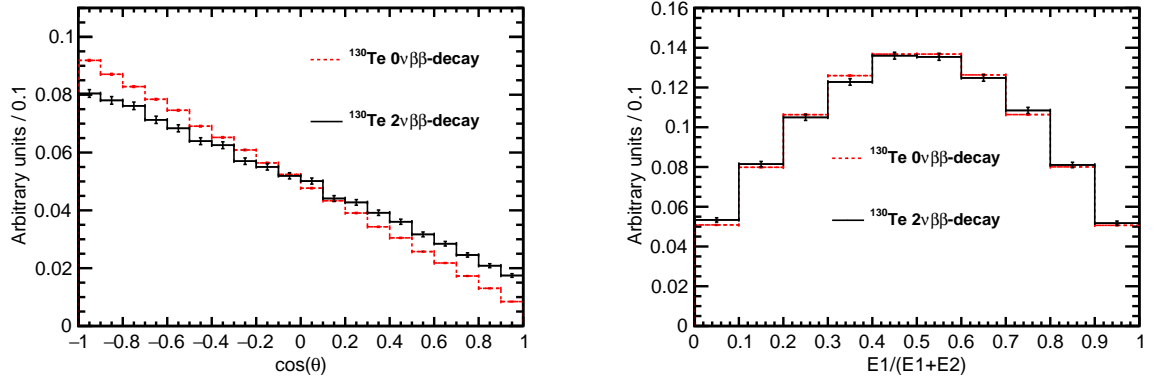


Figure 1: Comparison between kinematics of  $0\nu\beta\beta$  (dashed red lines) and  $2\nu\beta\beta$  decays (solid black lines) for events with the total kinetic energy of the electrons above 90% of the Q-value. *Left*: Cosine of the angle between two electrons. *Right*: Fraction of energy carried by one of the two electrons. Vertical bars at each bin of the histograms indicate statistical uncertainty for that bin.

Cherenkov light is produced.

Figure 2 shows the output of the detector simulation for 1000 simulated  $^{130}\text{Te}$   $0\nu\beta\beta$ -decay events. The left panel in Fig. 2 compares PE arrival time between Cherenkov and scintillation light and the right panel in Fig. 2 zooms in on the Cherenkov photon distribution which is key to direction and topographical reconstruction.

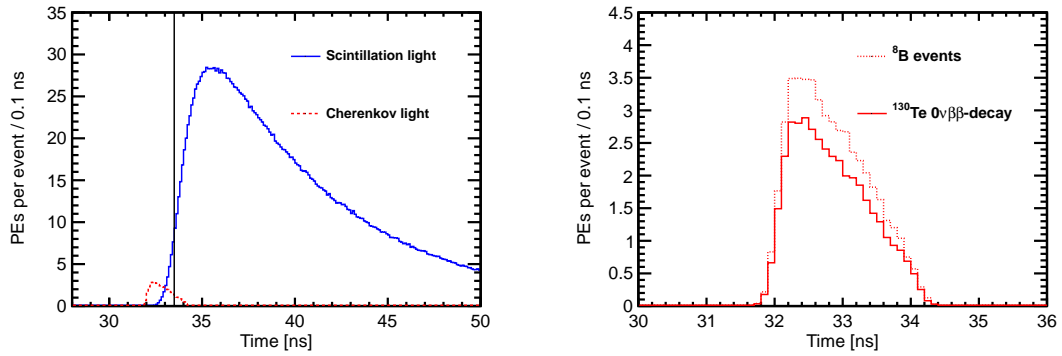


Figure 2: *Left*: Photo-electron (PE) arrival times after application of the photo-detector transit time spread (TTS) of 100 ps for the default simulation of  $^{130}\text{Te}$   $0\nu\beta\beta$ -decay produced at the center of the detector. Scintillation PE arrival time distribution is compared for  $\nu\beta\beta$ -decay (dashed blue line) and  $^{10}\text{C}$  events (dotted green line). The corresponding distribution for  $^8\text{B}$  events is not shown because it is indistinguishable from the distribution for  $\nu\beta\beta$ -decay. Cherenkov PE arrival times are shown for  $\nu\beta\beta$ -decay (solid red line) to demonstrate their contribution to the early PE sample. The vertical line at 33.5 ns indicates the time cut for the selection of the early PE sample. The shape of scintillation PE arrival times for  $^8\text{B}$  events *Right*: Comparison between Cherenkov PEs arrival time for  $^{130}\text{Te}$   $0\nu\beta\beta$ -decay (solid line),  $^8\text{B}$  (dashed line).

Selection of PEs with relatively small arrival time allows to select a sample of PEs with high fraction of directional Cherenkov light. This allows for event topology reconstruction. In particular, signal-like events with exactly two



electrons can be separated from events with only one electron such as from  $^8\text{B}$  solar neutrino interactions.

As shown in Fig. 2, for events produced at the center of the detector, a time cut of 33.5 ns on the PE arrival time selects a sample of early PEs that includes the majority of directional Cherenkov photons. Scintillation PEs also are selected with this time cut. Figure 3 shows the total number of scintillation and Cherenkov PE per event in the early PE sample for signal and background events.

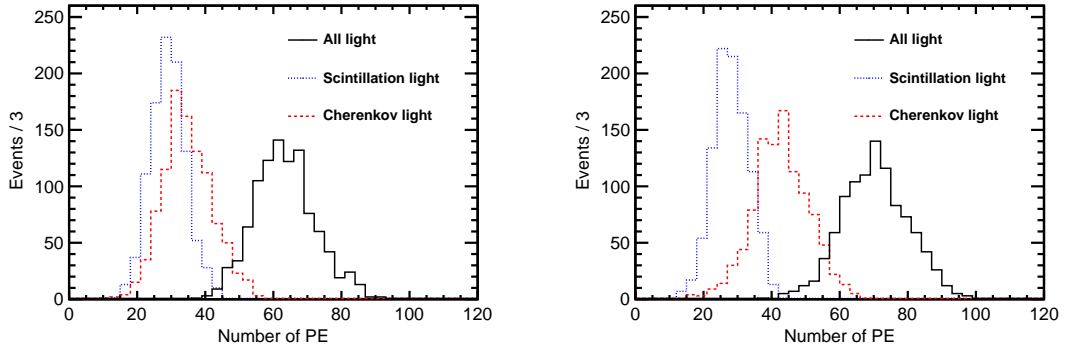


Figure 3: Early PE sample composition: number of Cherenkov (dashed red line), scintillation (dotted blue line), and total (solid black line) PEs per event for the simulation of 1000  $^{130}\text{Te}$   $0\nu\beta\beta$ -decay events (left panel), 1000  $^8\text{B}$  events (middle panel).

### 3.2. $^8\text{B}$ background

For a detector similar to our model  $^8\text{B}$  background is significant due to large mass.

Electrons from elastic scattering of  $^8\text{B}$  solar neutrinos have nearly flat energy spectrum around the Q-value [14].

We simulate  $^8\text{B}$  background as a single monochromatic electron with energy of 2.53 MeV (Q-value of  $^{130}\text{Te}$ ). A

2.53 MeV electron travels a total path length of 0.X cm, has a distance from the origin of 0.X cm in  $0.0X \pm 0.00X$  ns

and takes  $0.0X \pm 0.00X$  ns to drop below Cherenkov threshold.

The scintillation PE timing distribution is unchanged compared to  $0\nu\beta\beta$ -decay since the electron's path lengths at these energies are too short to affect the effective vertex of the scintillation light. The number of Cherenkov photons is increased (see Fig. 2 and 3) due to the increased electron kinetic energy but this alone is not sufficient to distinguish  $^8\text{B}$  events from  $0\nu\beta\beta$ -decay. However, it may provide an extra handle on signal-background separation in combination

<sup>149</sup> (e.g. by using multivariate techniques) with other event parameters.

## 4. Event Topology and Spherical Harmonics Analysis

In this section we provide details about spherical harmonics analysis to separate  $0\nu\beta\beta$ -decay signal events from  ${}^8\text{B}$  background. We show that spherical harmonics decomposition of the PE hits on the detector surface is sensitive to the differences between two-electron ( $0\nu\beta\beta$ -decay events) and single-electron ( ${}^8\text{B}$  events) topologies.

### 4.1. Topology of $0\nu\beta\beta$ -decay and ${}^8\text{B}$ Events

When a typical  $0\nu\beta\beta$ -decay candidate isotope is considered, all  ${}^8\text{B}$  background events will have that single electron above Cherenkov threshold in a liquid scintillator. Also a large fraction of  $0\nu\beta\beta$ -decay signal events will have both electrons above Cherenkov threshold. Cherenkov photons from each of the electrons will produce ring shaped clusters of PE hits on the detector surface. Therefore, any event reconstruction algorithm that is capable of separating events with one Cherenkov cluster from events with two Cherenkov clusters should have signal-background discrimination power.

In some cases only one Cherenkov cluster is produced in  $0\nu\beta\beta$ -decay signal events. This happens either when the angle between the two  $0\nu\beta\beta$ -decay electrons is small and Cherenkov clusters overlap or when the energy split between electrons is not balanced causing one electron to be below Cherenkov threshold. Such signal events cannot be separated from background based on topology of the Cherenkov photons distribution on the detector surface. However directionality of the electron that is above Cherenkov threshold can still be reconstructed. This directionality information would allow for  ${}^8\text{B}$  events suppression based on the position of the sun.

Identification of the Cherenkov clusters is challenging due to much higher amount of uniformly distributed scintillation light that is produced in every event. We found that spherical harmonics analysis on an early PE sample which has relatively high fraction of Cherenkov PE makes it possible to separate some of the  $0\nu\beta\beta$ -decay signal events from backgrounds.

## 4.2. Description of Spherical Harmonics Analysis

For the purpose of illustration of the spherical harmonics analysis concept we first consider three distinct topologies: two electrons produced back-to-back at an  $180^\circ$  angle, two electrons at a  $90^\circ$  angle, and a single electron. Figure 4 shows an idealized simulation of these three topologies for the total electrons energy of 10 MeV. In order to emphasize ring patterns formed by Cherenkov photons the electron multiple scattering process is turned off in this idealized simulation. Here the single-electron event represents an idealized  $^8\text{B}$  event topology and the two-electron events represent two special cases of an idealized  $0\nu\beta\beta$ -decay topology.

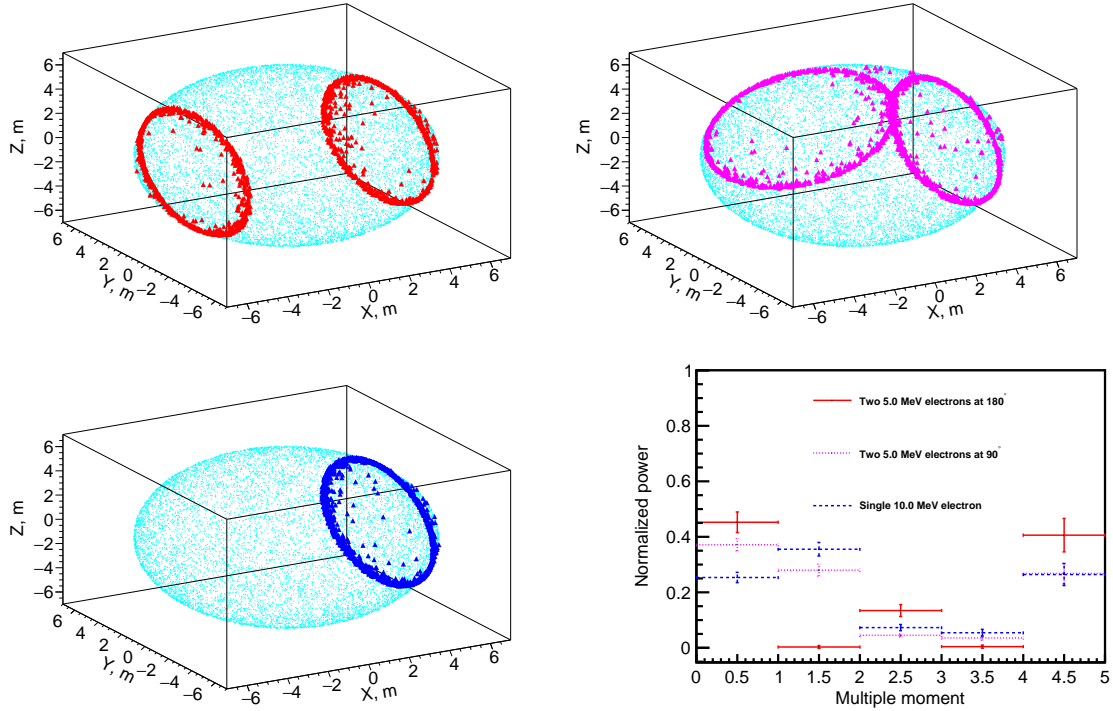


Figure 4: *Top panels and bottom left panel:* Idealized event displays for the three representative event topologies: two 5 MeV back-to-back electrons (*top left*), two 5 MeV electrons at  $90^\circ$  angle (*top right*), and a single 10 MeV electron (*bottom right*). Multiple scattering is turned off in the simulation to emphasize the difference in the mutual orientation of Cherenkov rings for the three topologies. For the illustration purposes 100% QE is applied to Cherenkov photons (triangles) and the default QE is applied to scintillation photons (dots). All electrons originate at the center of the detector. One typical event is shown for each topology. *Bottom right panel:* Normalized power spectrum  $S_l$  calculated for distribution of Cherenkov photons only. The three topologies are compared: two 5 MeV back-to-back electrons (*solid red line*), two 5 MeV electrons at  $90^\circ$  angle (*dotted magenta line*), and a single 10 MeV electron (*dashed blue line*). For each topology 100 events were simulated. The normalized power values  $S_l$ 's were calculated for each individual event. The horizontal lines correspond to the mean values of  $S_l$  within each event topology. The vertical bars show one standard deviation from the mean value.

The central strategy of the spherical harmonics analysis is to construct rotationally invariant variables that can be

179 used to separate different event topologies. To this end, let the function  $f(\theta, \phi)$  represent the PE distribution on the  
 180 detector surface. The function  $f(\theta, \phi)$  can be decomposed into a sum of spherical harmonics:

$$181 \quad f(\theta, \phi) = \sum_{l=0}^{\infty} \sum_{m=-l}^l f_{lm} Y_{lm}(\theta, \phi), \quad (1)$$

182 where  $Y_{lm}$  are Laplace's spherical harmonics defined in a real-value basis using Legendre polynomials  $P_l$ :

$$183 \quad Y_{lm} = \begin{cases} \sqrt{2} N_{lm} P_l^m(\cos\theta) \cos m\phi, & \text{if } m > 0 \\ N_{lm} = \sqrt{\frac{(2l+1)}{4\pi} \frac{(l-m)!}{(l+m)!}}, & \text{if } m = 0 \\ \sqrt{2} N_{l|m|} P_l^{|m|}(\cos\theta) \sin |m|\phi, & \text{if } m < 0 \end{cases} \quad (2)$$

184 where the coefficients  $f_{lm}$  are defined as

$$185 \quad f_{lm} = \int_0^{2\pi} d\phi \int_0^\pi d\theta \sin\theta f(\theta, \phi) Y_{lm}(\theta, \phi). \quad (3)$$

186 Equation 4 defines the power spectrum of  $f(\theta, \phi)$  in the spherical harmonics representation,  $s_l$ , where  $l$  is a multiple  
 187 moment. The power spectrum,  $s_l$ , is invariant under rotation. It is unique to each of the functions  $f_i(\theta, \phi)$ ,  $i=1,2,3,\dots$ ,  
 188 which can not be transformed into each other by rotation.

$$189 \quad s_l = \sum_{m=-l}^{m=l} |f_{lm}|^2 \quad (4)$$

190 The event topology in a spherical detector determines the distribution of the PE's on the detector sphere, and,  
 191 therefore, a set of  $s_l$ 's. These values can serve as a quantitative figure of merit for different event topologies. The

rotation invariance of  $s_l$ 's ensures that this figure of merit does not depend on the orientation of the event with respect to the chosen coordinate frame.

Sum of  $s_l$ 's over all multiple moments equals to the L2 norm of the function  $f(\theta, \phi)$ :

$$\sum_{l=0}^{\infty} s_l = \int_{\Omega} |f(\theta, \phi)|^2 d\Omega. \quad (5)$$

Therefore, the normalized power spectrum,

$$S_l = \frac{s_l}{\sum_{l=0}^{\infty} s_l} = \frac{s_l}{\int_{\Omega} |f(\theta, \phi)|^2 d\Omega}, \quad (6)$$

can be used to compare shapes of various functions  $f(\theta, \phi)$  with different normalization. The total number of PEs detected on the detector sphere fluctuates from event to event, therefore, in all of the following we use the normalized power  $S_l$ .

Figure 4((bottom right)) compares the normalized power spectra for the three representative event topologies. There is sufficient separation between these three idealized event topologies.

In practice, at energies relevant to  $0\nu\beta\beta$ -decay Cherenkov rings become very fuzzy due to electron multiple scattering. In most cases  $\sim 1$  MeV electrons produce randomly shaped clusters of Cherenkov photons around the direction of the electron track. Examples of such Cherenkov clusters for the same three representative topologies are shown in Fig. 5. Now the multiple scattering process is included in the simulation and the total kinetic energy of the electrons is equal to the Q-value of the  $^{130}\text{Te}$ .

At 2.53 MeV with multiple scattering included the difference in the Cherenkov photon distribution for the three representative topologies is not as dramatic as in the idealized simulation of 10 MeV events. However, a guess about

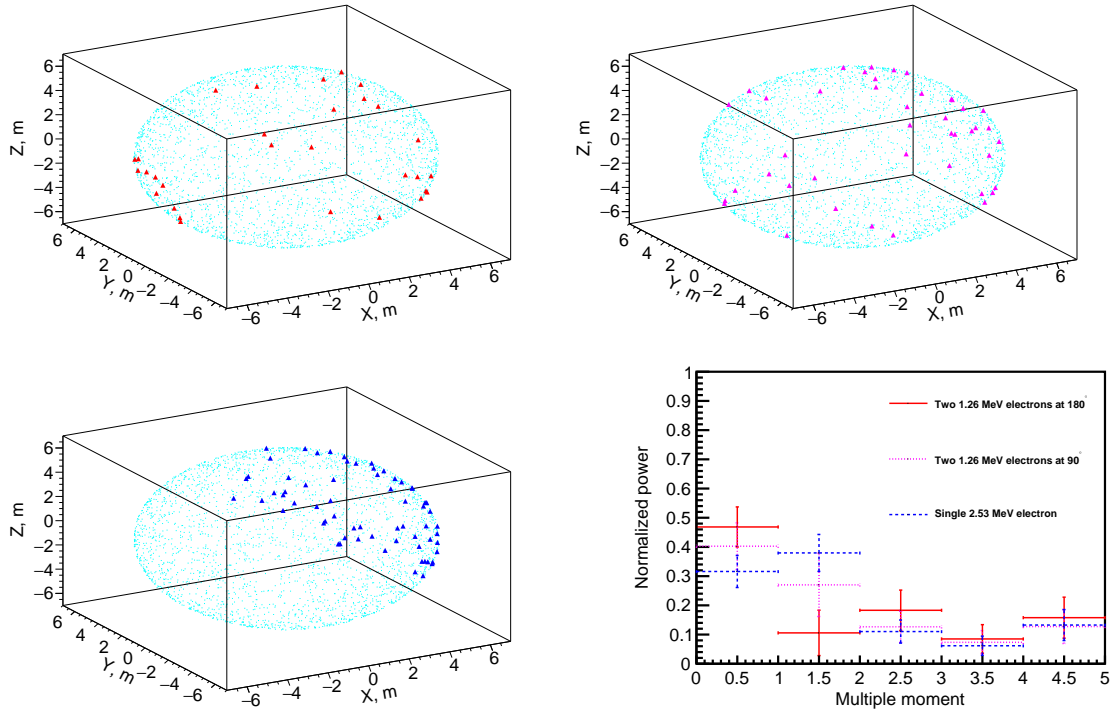


Figure 5: *Top panels and bottom left panel:* Event displays for the three representative event topologies with the electron energies relevant for the  $^{130}\text{Te}$   $0\nu\beta\beta$ -decay: two back-to-back 1.26 MeV electrons (*top left*), two 1.26 MeV electrons at  $90^\circ$  angle (*top right*), and a single 2.53 MeV electron (*bottom left*). Multiple scattering is now properly included in the simulation. For the illustration purposes 100% QE is applied to Cherenkov photons (triangles) and the default QE is applied to scintillation photons (dots). All electrons originate at the center of the detector. One typical event is shown for each topology. *Bottom right panel:* Normalized power spectrum  $S_l$  calculated for distribution of Cherenkov photons only. The three topologies are compared: two back-to-back 1.26 MeV electrons (*solid red line*), two 1.26 MeV electrons at  $90^\circ$  angle (*dotted magenta line*), and a single 2.53 MeV electron (*dashed blue line*). For each topology 1000 events were simulated. The normalized power values  $S_l$ 's were calculated for each individual event. The horizontal lines correspond to the mean values of  $S_l$  within each event topology. The vertical bars show one standard deviation from the mean value.

the event topology still can be made by comparing photon distributions in different segments of the detector sphere. Spherical harmonics decomposition is a natural tool for making such comparison between the segments. As shown in Fig. 5 (*bottom right*) spherical harmonics power spectrum of Cherenkov photons only still provides noticeable separation between all three event topologies.

More realistic examples of  $^{130}\text{Te}$   $0\nu\beta\beta$  and  $^8\text{B}$  events simulated at the center of the detector are shown in Fig. 6.  $^{130}\text{Te}$  events are generated based on the phase factors described in ?? .  $^8\text{B}$  events are implemented as monochromatic electrons with the initial direction along  $x$ -axis. Early photo-electrons (PEs), defined as those PEs from Cherenkov and scintillation light within 33.5 ns of the start of the event, are shown. The default QE is applied. In this more

218 realistic example, the uniformly distributed scintillation light makes it more difficult to visually distinguish the event  
 219 topology. Nevertheless, Fig. 6 (*bottom panel*) shows that the spherical harmonics analysis still finds differences  
 220 between two-track and single-track events.

221 As shown in the middle row of Fig. 6,  $0\nu\beta\beta$  events become indistinguishable from single-track events when the  
 222 angle between the two electrons is small and two Cherenkov clusters overlap. Event topologies of  $0\nu\beta\beta$  and  $^8\text{B}$  events  
 223 are also very similar when only one electron from  $0\nu\beta\beta$  is above the Cherenkov threshold. Therefore spherical  
 224 harmonics analysis is most efficient for events with large angular separation between the two electrons and when both  
 225 electrons are above Cherenkov threshold.

226 Being able to distinguish between two-tracks and single-track events using the spherical analysis can allow further  
 227 cuts to be made. For example, one might use absolute directional information to suppress single track events where  
 228 the direction of the track is consistent with the location of a known background such as the sun. Once a single track  
 229 topology is established, one can use a centroid method (see Ref. [? ]) to reconstruct directionality of the track (or two  
 230 degenerate tracks) in order to suppress events that are aligned with the direction of  $^8\text{B}$  solar neutrinos.

#### 231 4.3. Spherical Harmonics Analysis and Off-center Events

232 In general, the power spectrum  $S_l$  is rotation invariant for a given topology only if events originate in the center  
 233 of the detector. In order to compare spherical harmonics for events with vertices away from the center a coordinate  
 234 transformation for each photon hit is needed. The necessary transformation applied for each PE within an event is  
 235 illustrated in Fig. 7. The solid circle in Fig. 7 has a radius  $R$  and shows the actual detector boundaries. The dotted  
 236 circle shows a new sphere with the same radius  $R$ , which now has the event vertex in its center. The radius vector of  
 237 each PE is stretched or shorten to its intersection with this new sphere using the transformation,  $\vec{r}_{PE}^* = \frac{\vec{a}}{|\vec{a}|} \cdot R$ , where  
 238  $\vec{r}_{PE}^*$  is a new radius vector of a PE and  $\vec{a} = \vec{r}_{PE} - \vec{r}_{vtx}$  with  $\vec{r}_{PE}$  and  $\vec{r}_{vtx}$  being radius vectors of the PE and the vertex in



239 the original coordinates, respectively.

#### 240 4.4. *Implementation of the spherical harmonics analysis*

241 Numerical calculation of the power spectrum is implemented as follows. For each event, we create a 2-D his-  
242 togram,  $\theta$  vs  $\phi$ , with the distribution of PEs on the detector surface. We then treat this histogram as a function  $f(\theta, \phi)$   
243 where the value of the function for any pair of  $\theta$  and  $\phi$  is equal to the number of PE in the histogram bin corresponding  
244 to that pair.

245 Coefficients  $f_{lm}$  from Eq. 3 are calculated using a Monte Carlo integration technique. Variables  $S_l$ 's are calculated  
246 using Eqs.4 - 6. **Also need to provide reference to the libraries for Legendre polynomials.**

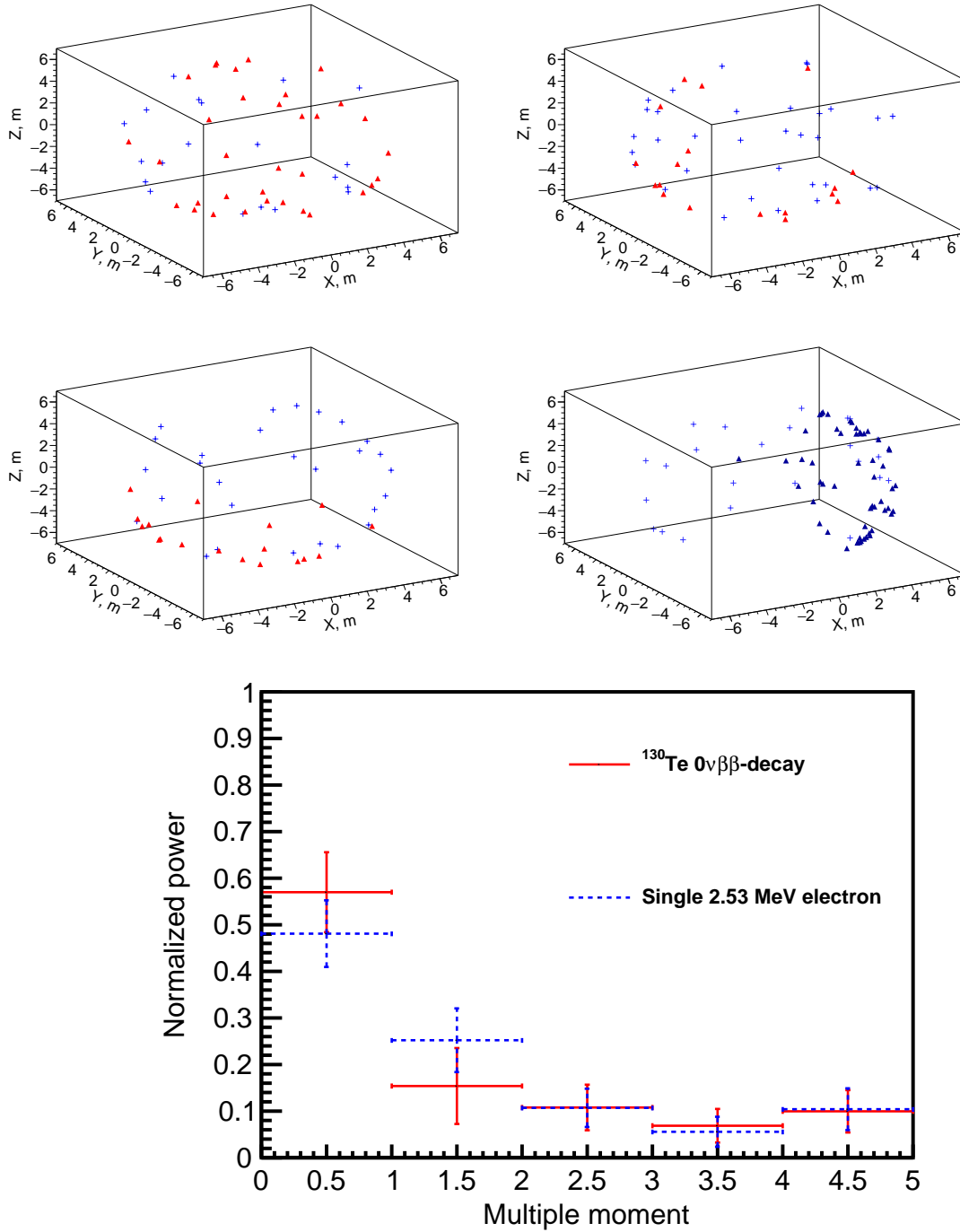


Figure 6: *Top and middle rows:* Event display examples for  $^{130}\text{Te}$   $0\nu\beta\beta$ -decay signal and  $^8\text{B}$  background events. The default QE and the time cut of 33.5 ns are applied to both Cherenkov (*triangles*) and scintillation (*crosses*) photons. For the  $^{130}\text{Te}$   $0\nu\beta\beta$ -decay signal three representative events are shown each closely matching on of the three topologies. A typical single electron event is shown for the  $^8\text{B}$  background. *Top left:*  $^{130}\text{Te}$   $0\nu\beta\beta$ -decay back-to-back electrons:  $E_1=1.257$  MeV,  $E_2=1.270$  MeV,  $\cos(\theta)=-0.908$ . *Top right:*  $^{130}\text{Te}$   $0\nu\beta\beta$ -decay electrons at  $\sim 90^\circ$ :  $E_1=1.264$  MeV,  $E_2=1.263$  MeV,  $\cos(\theta)=-0.029$ . *Middle left:*  $^{130}\text{Te}$   $0\nu\beta\beta$ -decay electrons at  $\sim 0^\circ$ :  $E_1=1.186$  MeV,  $E_2=1.340$  MeV,  $\cos(\theta)=0.888$ . *Middle right:* 2.529 MeV single electron. In all events electrons originate at the center of the detector. *Bottom panel:* Normalized power spectrum  $S_l$  calculated for distribution of all PE after the 33.5 ns time cut.  $^{130}\text{Te}$   $0\nu\beta\beta$ -decay signal (*solid red line*) and  $^8\text{B}$  background (*dashed blue line*) topologies are compared. Simulation of 1000 signal and background events. The normalized power values  $S_l$ 's were calculated for each individual event. The horizontal lines correspond to the mean values of  $S_l$ . The vertical bars show one standard deviation from the mean value.

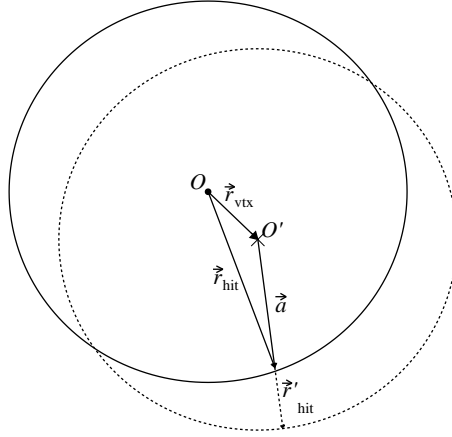


Figure 7: Coordinate transformation applied to events that are off-center. Solid circle schematically shows actual detector boundaries. Dotted circle shows a new sphere of radius  $R=6.5$  m with the event vertex position in the center. The radius vector of each photon hit is stretched or shorten until intersection with this new sphere using transformation  $\vec{r}_{hit}^* = \frac{\vec{d}}{|\vec{d}|} \cdot R$ . Where  $\vec{r}_{hit}^*$  is a new radius vector of the photon hit,  $R$  is detector sphere radius, and  $\vec{d} = \vec{r}_{hit} - \vec{r}_{vtx}$  with  $\vec{r}_{hit}$  and  $\vec{r}_{vtx}$  being radius vectors of the photon hit and vertex position in original coordinates and correspondingly.

## 5. Performance of the Spherical Harmonics Analysis in Separating $0\nu\beta\beta$ -decay from $^8\text{B}$ Background.

In this section we discuss factors that affect performance of the spherical harmonics analysis in separating  $0\nu\beta\beta$  signal from  $^8\text{B}$  background events. We found that most separation comes from the first two multiple moments,  $l = 0$  and  $l = 1$ . However, according to Eq. 6, higher multiple moments are needed for a better normalization of the power spectrum  $S_l$ . In the following we choose to calculate power spectrum  $s_l$  up to multiple moment of  $l=3$  and use only normalized variable  $S_0$  and  $S_1$ , where the normalization is given by

$$S_{0,1} = \frac{s_{0,1}}{\sum_{l=0}^3 s_l} \quad (7)$$

As discussed below, a linear combination of  $S_0$  and  $S_1$  can be used to construct a single variable,  $S_{01}$ , that provides separation between signal and background in 1-D space. We show distributions of this variable  $S_{01}$  to demonstrate qualitatively the separation between  $0\nu\beta\beta$  and  $^8\text{B}$  events depending on a few key assumptions about the detector characteristics.

Since the goal of this paper is to describe the technique of spherical harmonics analysis for separating different event topologies relevant for  $0\nu\beta\beta$ -decay searches in a generic liquid scintillator detector, we intentionally refrain from any quantitative estimates on the improvements in sensitivity to  $0\nu\beta\beta$  decay. The actual improvements in sensitivity due to spherical harmonics analysis would depend on various details of a given experimental setup. Therefore, we believe that detailed quantitative sensitivity studies are more appropriate in the context of a particular  $0\nu\beta\beta$  decay experiment which is beyond the scope of this paper.

### 5.1. Central events with perfect vertex reconstruction

We start evaluating the performance of the spherical harmonics analysis by looking at events that originate at the center of the detector and by assuming perfect reconstruction of the event vertex position. For such events, a time cut of 33.5 ns on PE's arrival time can be applied to obtain early PE's sample which contain high fraction of Cherenkov PE. The default QE and 100% photo-coverage is used in the simulation.

Comparison of  $S_0$  and  $S_1$  distributions for  $0\nu\beta\beta$ -decay signal and  ${}^8\text{B}$  background events is shown in Fig. 8. Both variables provide a noticeable separation between signal and background. We also note that in the energy range of interest, the  $S_l$ 's do not strongly depend on the energy deposited in the detector, which makes information contained in the normalized power spectrum complementary to the energy measurements. Therefore, spherical harmonics analysis can be used as an additional handle for background suppression at the end point of the  $0\nu\beta\beta$ -decay energy spectrum.

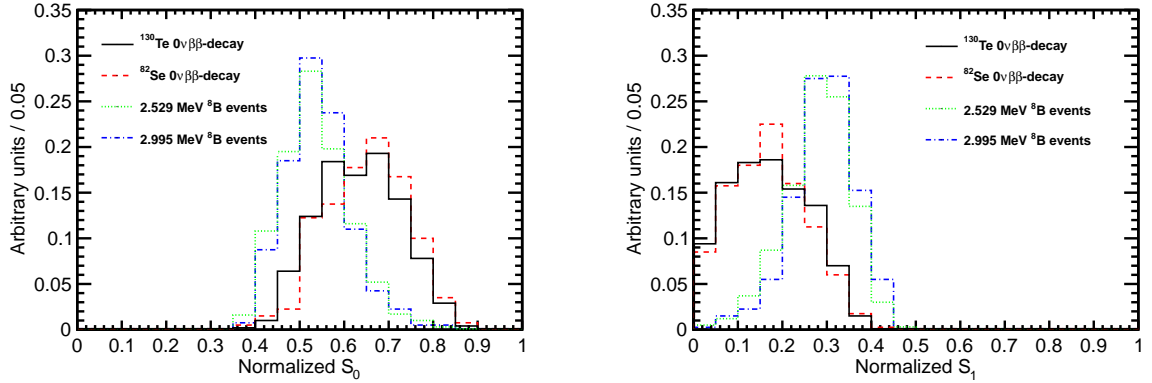


Figure 8:  $S_0$  (left) and  $S_1$  (right) distributions for 1000 simulated  $0\nu\beta\beta$ -decay signal and  ${}^8\text{B}$  background events. Two different isotopes are compared,  ${}^{130}\text{Te}$  and  ${}^{82}\text{Se}$ . Corresponding kinetic energies of  ${}^8\text{B}$  single electrons are 2.53 MeV and 3.00 MeV. Central events assuming perfect reconstruction of vertex position. Time cut of 33.5 ns on the PE arrival time is applied. The default QE and 100% photo-coverage is used in the simulation.

Left panel in Fig. 9 compares scatter plots of the first two components of the power spectrum,  $S_0$  and  $S_1$ , for signal and background. In order to optimize separation between  ${}^{130}\text{Te}$  and  ${}^8\text{B}$  events, a linear combination of variables  $S_0$  and  $S_1$  is constructed as follows.

First, a linear fit,  $S_0 = A \cdot S_1 + B$ , of all points on the scatter plot is performed as shown by the dashed line in the left panel in Fig. 9. Then a 1-D variable  $S_{01}$  is defined as  $S_{01} = S_1 \cdot \cos(\theta) + S_0 \cdot \sin(\theta)$ , where  $\tan(\theta)=A$ . Right panel in Fig. 9 compares distributions of  $S_{01}$  for  $0\nu\beta\beta$ -decay signal and  $^8\text{B}$  background. These 1-D histograms for  $S_{01}$  represent projection of the points on the scatter plot onto the fitted line. We use distribution of the variable  $S_{01}$  as a figure of merit for signal/background separation. Figure 9 demonstrates that spherical harmonics analysis potentially brings extra separation power which is in addition to the energy measurements.

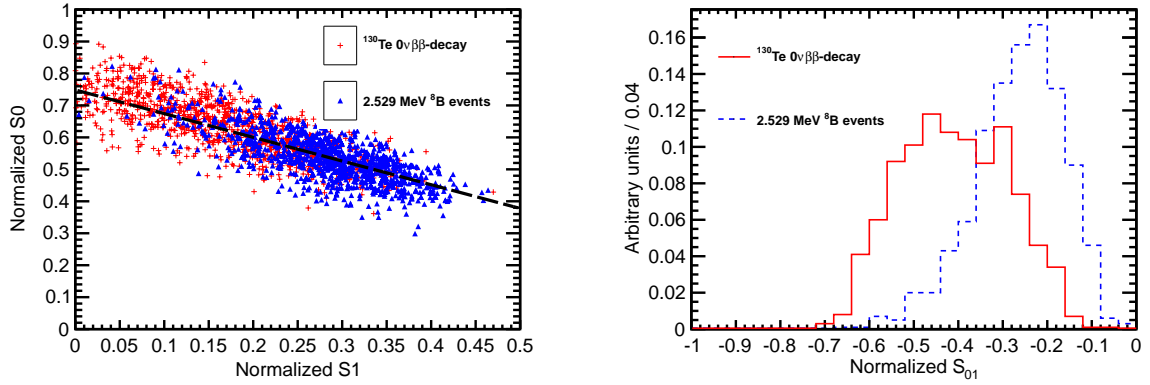


Figure 9: *Left*: Scatter plot of  $S_0$  versus  $S_1$  for a simulation of 1000 signal (red crosses) and background (blue triangles) events. Central events assuming perfect reconstruction of vertex position. Time cut of 33.5 ns on the PE arrival time is applied. The default QE and 100% photo-coverage is used in the simulation. Black dashed line corresponds to a linear fit to define 1-D variable  $S_{01}$  (see text for details). *Right*: Comparison of the  $S_{01}$  distribution between signal (red solid line) and background (blue dashed line).

## 5.2. Experimental challenges

So far only events at the center of the detector have been considered. Precise vertex reconstruction has been also assumed. Here we discuss performance of the spherical harmonics analysis for events that originate throughout the whole fiducial volume of the detector and that also have limited vertex reconstruction precision.

Selection of early PE sample using absolute time cut of 33.5 ns that has been applied to central events relies on the fact that, within the uncertainty on electron track length, all photons travel the same distance before reaching the surface of the detector. PEs with early measured time correspond mostly to Cherenkov photons because of the delay in the scintillation process and longer wavelength of the Cherenkov light.

When the vertex is not at the center, a uniform absolute time cut on the photon arrival time is no longer effective in selecting Cherenkov photons. In the case of an off-center vertex, there could be a situation when even significantly delayed scintillation photons reach the side of the detector that is closer to the vertex much earlier than Cherenkov photons traveling to the opposite side of the detector. Therefore, the time cut has to take into account the total distance traveled by each individual photon.

We found that a differential time cut defined as  $\Delta t = t_{measured}^{phot} - t_{predicted}^{phot} < 1$  ns selects photons with a sufficient fraction being Cherenkov photons. However, when this differential time cut is applied, two factors significantly reduce the Cherenkov/scintillation light separation in the early PE sample, and therefore, reduce discrimination power of the spherical harmonics analysis. These factors are chromatic dispersion and vertex resolution. In the following we describe both effects and propose solutions to mitigate their influence on the spherical harmonics analysis.

### 5.2.1. Chromatic dispersion

One reduction in the Cherenkov/scintillation light separation comes from chromatic dispersion. The predicted time,  $t_{predicted}^{phot} = l/v^{phot}$ , depends on the distance,  $l$ , traveled by the photon and the velocity of the photon,  $v^{phot}$ . Since the wavelength information is not available for a given PE, we must use an average index of refraction,  $n$ , and define the photon velocity as  $v^{phot} = c/n$ . This uncertainty on the photon velocity makes the differential time cut less effective in separating Cherenkov light from scintillation light.

Poor Cherenkov/scintillation light separation reduces the effectiveness of the spherical harmonics analysis. For each event topology spherical harmonics power spectrum is mostly determined by distinct distributions of Cherenkov photons. At the same time scintillation photons represent uniform background noise for event topology reconstruction.

In general, selection of an early PE sample for any event within a fiducial volume of a reasonable size has to be done with a time cut that would be affected by chromatic dispersion. We define fiducial volume as  $R < 3$  m, where

$R$  is the distance between event vertex and the center of the detector. Figure 10 demonstrates performance of the spherical harmonics analysis for events within this fiducial volume. Perfect vertex reconstruction is still assumed for events shown in Fig. 10. A differential time cut of 1 ns is used. Reduced separation between signal and background on Fig. 10 compared to Fig. 9 is due to the effect of chromatic dispersion which does not allow to achieve as high fraction of Cherenkov PEs in the early PE sample as in the case of central events when an absolute time cut of 33.5 ns is used.

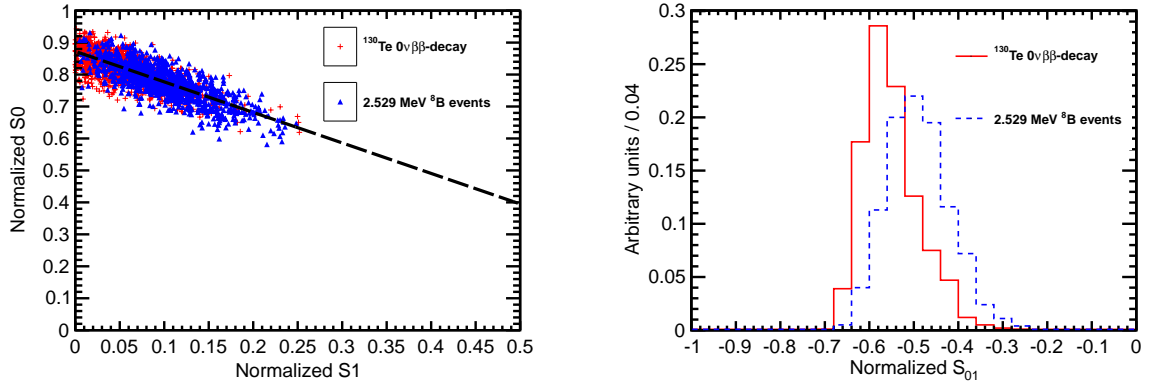


Figure 10: *Left*: Scatter plot of  $S_0$  versus  $S_1$  for a simulation of 1000 signal (red crosses) and background (blue triangles) events. Event vertices are uniformly distributed within the fiducial volume,  $R < 3$  m. Perfect reconstruction of the vertex position is assumed. Differential cut of  $\Delta t = t_{\text{measured}}^{\text{phot}} - t_{\text{predicted}}^{\text{phot}} < 1$  ns is applied to select early PE sample. The default QE and 100% photo-coverage is used in the simulation. Black dashed line corresponds to a linear fit to define 1-D variable  $S_{01}$  (see text for details). *Right*: Comparison of the  $S_{01}$  distribution between signal (red solid line) and background (blue dashed line).

### 5.2.2. Vertex resolution

Imprecise knowledge of the vertex position affects the spherical harmonics analysis in two ways. First, similarly to the effect of chromatic dispersion, the vertex uncertainty makes the differential time cut less efficient in separating Cherenkov and scintillation light. An uncertainty on the vertex position leads to an uncertainty on the photon predicted travel time,  $t_{\text{predicted}}^{\text{phot}}$ , which in turn increases the probability to mix scintillation and Cherenkov light in the early PE sample.

Second, in the case of single electron event topology, a small error in vertex reconstruction could cause a large



effect on the normalized power spectrum of spherical harmonics.

Early PE sample of the single electron topology typically has a strong asymmetry due to preferential directionality of Cherenkov PEs that are selected together with uniformly distributed scintillation PEs. A mis-reconstructed vertex introduces an artificial asymmetry in the selection of scintillation PE. Vertex shifts parallel to the direction of the electron track have the largest effect compared to the shifts in the transverse direction.

If a vertex is shifted in the direction opposite to the track of the electron, the differential time cut selects more scintillation photons that are emitted in the direction of the electron track. Therefore scintillation photons would enhance forward asymmetry of the early PE sample, which in turn, would move  $S_1$  to higher values<sup>1</sup>.

If a vertex is shifted in the same direction as the direction of the electron, the differential time cut selects more scintillation photons that are emitted in the direction opposite to the electron track. Therefore, the asymmetry of Cherenkov PEs would be counter balanced by scintillation PEs, which in turn, would move  $S_1$  to lower values.

Figure 11 shows the performance of the spherical harmonics analysis for events simulated in the entire fiducial volume with vertex reconstruction resolution of 3 cm. The vertex resolution is implemented as a substitution of the actual vertex position with a variable that has Gaussian smearing around the actual position along all three  $x$ -,  $y$ -, and  $z$ - directions around the actual position. The smearing is done with three independent Gaussian distributions that have the same width,  $\sigma_x = \sigma_y = \sigma_z = 3$  cm.

As can be seen in Fig. 11, the vertex resolution effect significantly reduces discrimination power of the spherical harmonics analysis in our default detector model.

---

<sup>1</sup>In general,  $S_1$  component of the spherical harmonics power spectrum is higher for asymmetric distributions and lower for symmetric distributions (e.g., compare back-to-back and single electron topologies in Fig. 4). Moreover,  $S_1 = 0$  for a distribution with perfect symmetry with respect to the center of the sphere.

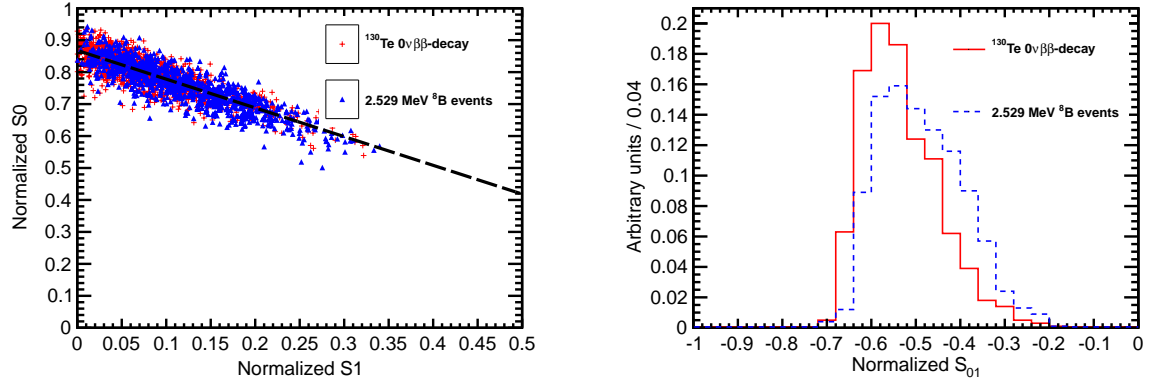


Figure 11: *Left:* Scatter plot of  $S_0$  versus  $S_1$  for a simulation of 1000 signal (red crosses) and background (blue triangles) events. Event vertices are uniformly distributed within the fiducial volume,  $R < 3$  m. Vertex is smeared with 3 cm resolution. Differential cut of  $\Delta t = t_{\text{measured}}^{\text{phot}} - t_{\text{predicted}}^{\text{phot}} < 1$  ns is applied to select early PE sample. The default QE and 100% photo-coverage is used in the simulation. Black dashed line corresponds to a linear fit to define 1-D variable  $S_{01}$  (see text for details). *Right:* Comparison of the  $S_{01}$  distribution between signal (red solid line) and background (blue dashed line).

### 5.3. Requirements for the next generation liquid scintillator detectors

To take full advantage of topology reconstruction capabilities in the next generation liquid scintillator detectors optical properties of the scintillator has to be tuned to allow for better Cherenkov/scintillation light separation.

The effects due to chromatic dispersion can be addressed by using liquid scintillators with a more narrow emission spectrum. For example, such as described in Ref. [?] .

Strong dependence on the vertex resolution can be addressed by choosing a liquid scintillator mixture with a more delayed emission of scintillation light with respect to Cherenkov light. With a larger delay in scintillation light, a high fraction of Cherenkov light can be maintained in the early PE sample even if photon track length is misreconstructed due to imprecise reconstruction of the vertex position. In addition, if the fraction of scintillation light is small compared to Cherenkov light, the distortions in the uniformity of the scintillation PE due to shifted reconstructed vertex position would not significantly affect spherical harmonics power spectrum.

While our default detector model assumes scintillation rise time of  $\tau_r = 1$  ns, scintillation rise time up to  $\tau_r = 7$  ns can be achieved (see Ref. ??). As a test we repeated spherical harmonics analysis on  $0\nu\beta\beta$ -decay and  ${}^8\text{B}$  events after

increasing scintillation rise time parameter to  $\tau_r = 5$  ns in our detector model. All other parameters are kept the same.

Figure 12 shows result of that test. The events are uniformly distributed within the fiducial volume and each vertex is smeared with 3 cm resolution.

We conclude that a rise time of  $\tau_r = 5$  ns provides sufficient delay between Cherenkov and scintillation light to make spherical harmonics analysis a potentially useful technique to separate  $0\nu\beta\beta$ -decay signal from  ${}^8\text{B}$  background.

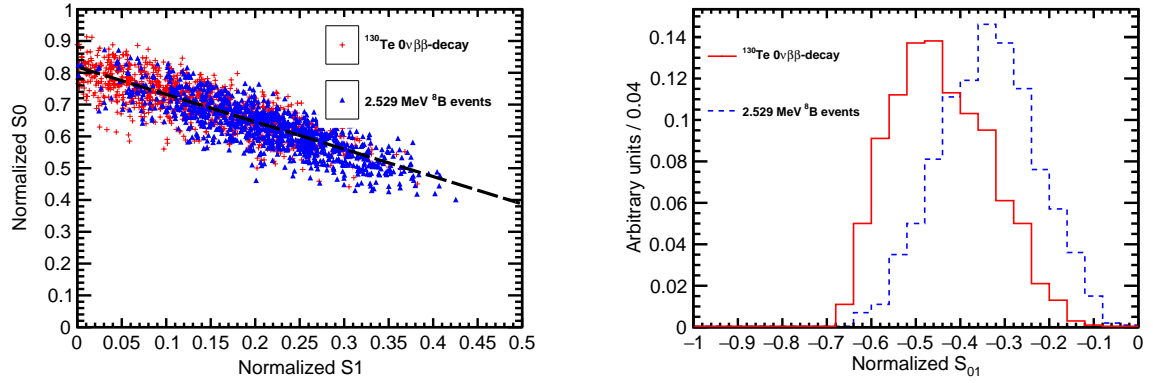


Figure 12: Scintillation rise time constant is increased to  $\tau_r = 5$  ns compared to  $\tau_r = 1$  ns in the default detector model. *Left:* Scatter plot of  $S_0$  versus  $S_1$  for a simulation of 1000 signal (red crosses) and background (blue triangles) events. Event vertices are uniformly distributed within the fiducial volume,  $R < 3$  m. Vertex is smeared with 3 cm resolution. Differential cut of  $\Delta t = t_{\text{measured}}^{\text{phot}} - t_{\text{predicted}}^{\text{phot}} < 1$  ns is applied to select early PE sample. The default QE and 100% photo-coverage is used in the simulation. Black dashed line corresponds to a linear fit to define 1-D variable  $S_{01}$  (see text for details). *Right:* Comparison of the  $S_{01}$  distribution between signal (red solid line) and background (blue dashed line).

## 6. Conclusions

A technique based on spherical harmonics analysis can separate  $0\nu\beta\beta$  decay from  $^8\text{B}$  solar neutrino interactions. The separation is based on the distinct event topologies of signal and background. This event topology information is available in addition to the measurements of the energy deposited in the detector. This technique may be further developed and adopted by future large scale liquid scintillator detectors to suppress background coming from  $^8\text{B}$  solar neutrino interactions in the detector volume. The performance of the technique is mostly affected by chromatic dispersions, vertex reconstruction and the time profile of the emission of scintillation light. We show that a liquid scintillator detector with a scintillation rise time constant  $\tau_r = 5$  ns provide sufficient cherenkov-scintillation light separation and potentially allows for use of the spherical harmonics analysis as an extra handle to extract  $0\nu\beta\beta$  decay signal.

## Acknowledgements

This work was supported by DOE grant number A, and NSF grant number B.

We thank Gabriel Orebi Gann of University of California, Berkeley for discussion on expected backgrounds at SNO+ experiment. We thank Jenni Kotilla of Yale for discussions on electron angular correlations in  $0\nu\beta\beta$ -decay and for providing data with phase factors for generating  $0\nu\beta\beta$ - and  $2\nu\beta\beta$ -decay events. We are grateful to Christoph Aberle, formerly at UCLA, for initial development of Geant-4 detector model used at this paper and early contribution to the development of Cherenkov/scintillation light separation technique. We thank Matthew Wetstein of the Iowa State University for help with vertex reconstruction algorithms and productive discussion on Cherenkov/scintillation light separation (**unless Matt wants to be an author**). We thank Eric Spiegler of the University of Chicago for productive discussions on spherical harmonics analysis. We also thank Evan Angelico of the University of Chicago for estimating effects of photo-detector position and time resolution on the vertex reconstruction and verifying effects of chromatic dispersions. We thank Carla Pilcher of the University of Chicago for discussions on gammas interactions in liquid scintillators. We thank Davide Franco of CNRS and Paolo Crivelli of ETH, Zurich for sharing their experience with ortho-positronium simulation in Geant-4. We thank Jan Flusser of Institute of Information Theory and Automation, Czech Academy of Sciences for helpful discussions on image processing using moment invariants. Last but not least we thank Mingfang Yeh of Brookhaven National Laboratory for discussions of timing properties of various liquid scintillators.

## References

- [1] Q. R. Ahmad, et al., Phys. Rev. Lett. 87 (2001) 071301.
- [2] K. Eguchi, et al., Phys. Rev. Lett. 90 (2003) 021802.
- [3] Q. R. Ahmad, et al., Phys. Rev. Lett. 89 (2002) 011301.
- [4] S. Fukuda, et al. (Super-Kamiokande), Phys. Lett. B 539 (2002) 179–187.
- [5] E. Majorana, Nuovo Cim. 14 (1937) 171–184.
- [6] M. Gell-Mann, P. Ramond, R. Slansky, Conf. Proc. C790927 (1979) 315–321.
- [7] T. Yanagida, Proc. of the Workshop on Unified Theory and the Baryon Number of the Universe Japan (1979).
- [8] M. Fukugita, T. Yanagida, Baryogenesis without grand unification, Phys. Lett. B 174 (1986) 45 – 47.
- [9] M. A. Luty, Phys. Rev. D 45 (1992) 455.

- [10] W. H. Furry, Phys. Rev. 56 (1939) 1184–1193.
- [11] M. Goeppert-Mayer, Phys. Rev. 48 (1935) 512–516.
- [12] A. Gando, et al. (KamLAND-Zen), Phys. Rev. Lett. 110 (2013) 062502.
- [13] S. D. Biller, Phys. Rev. D 87 (2013) 071301.
- [14] A. Maio (SNO+), Search for Majorana neutrinos with the SNO+ detector at SNOLAB, J. Phys. Conf. Ser. 587 (2015) 012030.
- [15] C. Aberle, A. Elagin, H. J. Frisch, M. Wetstein, L. Winslow, J. Instrum. 9 (2014) P06012.
- [16] S. Agostinelli, et al. (GEANT4), GEANT4: A Simulation toolkit, Nucl. Instrum. Meth. A506 (2003) 250–303.
- [17] J. Allison, et al., Geant4 developments and applications, Nuclear Science, IEEE Transactions on 53 (2006) 270–278.
- [18] O. Tajima, *Development of Liquid Scintillator for a Large Size Neutrino Detector*, Master’s thesis, Tohoku University, 2000.
- [19] O. Perevozchikov, *Search for electron antineutrinos from the sun with KamLAND detector*, Ph.D. thesis, University of Tennessee, 2009.
- [20] C. Grant, A Monte Carlo Approach to  $^7\text{Be}$  Solar Neutrino Analysis with KamLAND, Ph.D. thesis, University of Alabama, 2012.
- [21] C. Aberle, Optimization, simulation and analysis of the scintillation signals in the Double Chooz experiment, Ph.D. thesis, University of Heidelberg, 2011.
- [22] O. Tajima, *Measurement of Electron Anti-Neutrino Oscillation Parameters with a Large Volume Liquid Scintillator Detector, KamLAND*, Ph.D. thesis, Tohoku University, 2003.
- [23] Hamamatsu Photonics K.K., Large Photocathode Area Photomultiplier Tubes (data sheet, including R7081), 2013. [http://www.hamamatsu.com/resources/pdf/etd/LARGE\\_AREA.PMT.TPMH1286E05.pdf](http://www.hamamatsu.com/resources/pdf/etd/LARGE_AREA.PMT.TPMH1286E05.pdf).
- [24] Y. Abe, et al. (Double Chooz), Reactor electron antineutrino disappearance in the Double Chooz experiment, Phys. Rev. D86 (2012) 052008.
- [25] H. Grabas, R. Obaid, E. Oberla, H. Frisch, J.-F. Genat, R. Northrop, F. Tang, D. McGinnis, B. Adams, M. Wetstein, {RF} strip-line anodes for psec large-area mcp-based photodetectors, Nucl.Instrum.Meth. A 711 (2013) 124 – 131.
- [26] Oberla, E. and Genat, J. and Grabas, H. and Frisch, H. and Nishimura, K. and Varner, G., A 15 GSa/s, 1.5 GHz Bandwidth Waveform Digitizing ASIC, Nucl.Instrum.Meth. A735 (2014) 452–461.
- [27] B. Adams, et al., Invited article: A test-facility for large-area microchannel plate detector assemblies using a pulsed sub-picosecond laser, Review of Scientific Instruments 84 (2013) 061301.
- [28] B. Adams, et al., Measurements of the gain, time resolution, and spatial resolution of a  $20\times 20\text{cm}^2$  MCP-based picosecond photo-detector, Nucl.Instrum.Meth. A732 (2013) 392–396.
- [29] O. Seigmund, et al., Large area event counting detectors with high spatial and temporal resolution, J. Instrum. 9 (2014) C04002.
- [30] B. Adams, et al., An internalALD-basedhighvoltagedividerandsignalcircuit for MCP-basedphotodetectors, Nucl.Instrum.Meth. A780 (2015) 107–113.
- [31] B. Adams, et al., Timing characteristics of Large Area Picosecond Photodetectors, Nucl.Instrum.Meth. A795 (2015) 1–11.
- [32] M. Minot, et al., Pilot production & commercialization of LAPPD<sup>TM</sup>, Nucl.Instrum.Meth. A787 (2015) 78–84.